Turbulent Pressure Field in a Co-Annular Jet

R. J. Hammersley* and B. G. Jones†
University of Illinois at Urbana-Champaign, Urbana, Ill.

Single-point and two-point fluctuating static pressure measurements have been made in the initial mixing and transition regions in a co-annular circular jet. Space scales, correlation and time scales in the convected frame, and convection velocities have been determined for both broad-band and narrow-band frequency components. Analytical functionals describing the structural behavior of the turbulent pressure field have been developed from the data which are suitable for direct application in predicting the sound power level radiated from this turbulent field. Effects of both area and velocity ratios are incorporated in the model.

Nomenclature

A	= anisotropy factor
b	= mixing layer width
BB	= broad band
d_c, d_{Bp}	= diameter of core or of bypass nozzle
K_x, K_y, K_z	= decay coefficients in axial, radial, and lateral directions, respectively
L_p^x	= broad-band axial length scale for pressure
$\text{L}_{\text{p}}^y(\eta_0), L_p^z(\eta_0)$	= narrow-band radial and lateral length scale for pressure
L_{vv}^y	= radial velocity component radial integral length scale
p	= fluctuating pressure
p'	= rms fluctuating pressure
r	= velocity ratio, $\bar{U}_1/\bar{U}_2$ or $\bar{U}_{\text{Bp}}/\bar{U}_c$
R	= jet radius
R_{pp}	= pressure correlation coefficient
$R^L{}_{pp}(\eta_0, \tau)$	= narrow-band convected frame autocorrelation
t	= real time
T_p	= pressure convected frame integral time scale
$\bar{U}$	= local mean fluid velocity
$\bar{U}_1, \bar{U}_2$	= mean fluid velocity of inner and outer nozzles, respectively
$\bar{U}_{C_x}(\text{BB})$	= broad-band convection velocity for pressure
v'	= rms fluctuating radial velocity
x, y, z	= axial, radial, and lateral coordinates
$\Delta x, \Delta y, \Delta z$	= axial, radial, and lateral sensor separations
x_0	= virtual origin
α	= fit parameter, Eq. (1)
ϵ_y	= radial probe offset
η_0	= center-band frequency
λ	= wavelength of periodicity
λ_c	= wavelength scale constant
ρ	= fluid density
τ	= delay time

Superscripts

L	= convected frame
y	= radial component
$-$	= long time average
$'$	= root mean square (rms)

Subscripts

BP (Bp)	= bypass (outer nozzle)
c	= core nozzle or convection
max	= maximum value
p, pp	= pressure
$T\text{-}M$	= turbulent-mean shear interaction contribution
v	= radial coordinate component
x, y, z	= axial, radial, and lateral coordinate components

Presented as Paper 75-95 at the AIAA 13th Aerospace Sciences Meeting, Pasadena, Calif., January, 20-22, 1975; submitted January 27, 1975; revision received May 30, 1975. This work was sponsored under grant NASA NGR 14-005-177 and the University of Illinois.

Index categories: Jets, Wakes, and Viscid-Inviscid Flow Interactions; Aircraft Noise, Aerodynamics (Including Sonic Boom); Subsonic and Transonic Flow.

*Research Assistant in Nuclear Engineering, currently with Sargent and Lundy Engineers, Chicago, Ill.

†Professor of Nuclear and of Mechanical Engineering. Member AIAA.

I. Introduction

THE turbulent characteristics of a co-annular nozzle configuration have been studied in detail by Hammersley.[1] The final objective of this study was the prediction of the far-field noise produced by the turbulent flowfield in such jets. Ribner[2] formulated this problem in terms of the hydrodynamic pressure in the jet flow. The cross covariance of the hydrodynamic pressure field was shown to be the source term for the production of the far-field acoustic pressure. The detail structure of the velocity and pressure fields must first be ascertained before Ribner's formulation can be utilized. This paper examines specifically the turbulent structure of the pressure field of a co-annular jet flow.

II. Experimental Facilities

Flowfield Configuration and Operating Conditions

The general flowfield is illustrated in Fig. 1. It is important to notice three distinct flow zones. In the initial zone, there are two driven shear layers, which are followed by a transitional mixing region. This second zone results from the dissipation of the outer potential core prior to the dissipation of the inner potential core. The final zone, a transition region, is produced once both potential cores have dissipated.

The specific flow conditions investigated herein were subsonic and isothermal. The inner core nozzle velocity was 450 fps and the bypass nozzle velocity was adjusted to study velocity ratios ranging from 0.0 to 0.8. The core nozzle diameter was 3.0 in. and two bypass nozzles were employed: 1) 5.35 in. (area ratio of 2.2) and 2) 8.7 in. (area ratio of 7.4). The nozzles were always placed in a coplanar configuration. The experiments were performed at NASA Lewis Research Center, Cleveland, Ohio on an outdoor test facility. A schematic of the co-annular test facility is presented in Fig. 2.

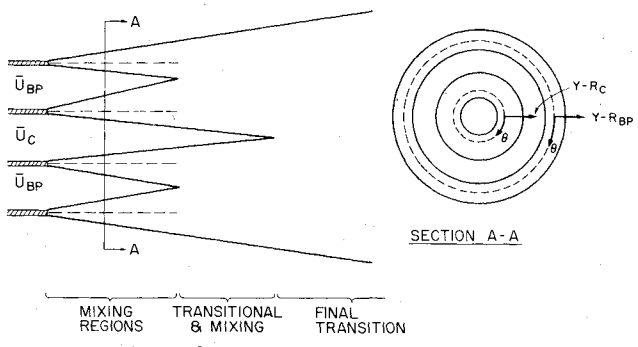

Fig. 1 General co-annular nozzle flowfield.

Instrumentation and Techniques

The fluctuating pressure field was monitored by using a miniature pressure transducer. The pressure instrument employs a constant-pressure air bleed past a hot-film sensor to follow the static pressure fluctuations in the flowfield. This instrument is used in conjunction with standard constant-temperature anemometry and produces a linear response to pressure variation without the use of a linearizer. Planchon[3] has described the construction and operation details of this device, including specific calibration procedures and method used to determine the instrument's transfer function. He also presented a detailed error analysis which shows that velocity induced errors in the measured pressure intensity are $\leq 4.5\%$.

The two-point structure of the turbulence was studied by using two matched pressure transducers. The transducers were matched to insure that they had the same frequency response characteristics and sensitivities to pressure fluctuations. The frequency response was corrected to be flat up to 10 kHz by using a simple resistance-capacitance circuit in series with the anemometer output. The phase shift between the instruments was negligible for all but the highest frequencies, which showed a less than 10° shift. The lack of phase shift was substantiated by two-point correlation measurements for probes placed adjacent to each other. Such measurements displayed no shift in the cross-correlation.

The experimental data was recorded on an FM tape system with a frequency bandwidth of d.c. to 20 kHz (±0.5 dB). The single-point pressure intensity variation simply required the appropriate conversion of the measured rms voltages to engineering units. The space-time correlations were computed by a T.S.I. Model 1065 (Honeywell-Saicor Model 42A) correlation and probability analyzer. This special-purpose digital computer used a lag-product-type algorithm in sampling, quantizing, multiplying, and adding products in 100 bins, corresponding to 100 equal lag times. A sufficient number of ensembles ranging from 128×1024 to 320×1024 was used to provide smooth correlation functions. This technique was used to produce both broad-band and narrow-band space-time correlations. The latter were found by passing the signals through 1/7 octave bandpass filters prior to correlating them. The filters were matched at the desired center frequency η_0 by correlating their response to a parallel input test signal.

III. Results and Discussion

Single-Point Fluctuating Pressure Intensity

The existence of the three distinct flow zones produced by a co-annular nozzle is clearly reflected in Fig. 3. This figure shows the evolution of the radial pressure intensity profiles as one moves downstream. In the region where both mixing regions exist there are two "humps" in the profile. As one proceeds downstream, the "valley" between the "humps" is diminished as the outer potential core dissipates. In the transitional-mixing zone only one peak is observed but the outer extreme of the profile still shows the effect of the outer mixing region. Finally, the final transition region is reached and the peak pressure intensity begins to decline. The profiles in Fig. 3 are for traverses originating outside the flow and extending to the centerline of the inner nozzle.

If the profiles for the several axial positions for each mixing region are cast into a similarity coordinate, Fig. 4 results. The similarity co-ordinate is $(y\text{-}R)\ /\ (x\text{-}x_0)$ where: y is the radial position, R is the jet radius, x is the axial position and x_0 is the virtual origin. The curves do not collapse but instead show an increase in magnitude for the length of the mixing region. However, the shape of the profile is essentially uniform and is adequately described by

$$p'/p'_{\max} = \exp[\alpha^2(\ (y-R)/(x-x_0)\ )^2] \qquad (1)$$

where α = empirical fit parameter which accomodates the spread of the mixing layer, p' = rms of the pressure fluctuations, $p'_{\max}$ = local maximum rms of the pressure fluctuations.

The interrelationship of the pressure and velocity fields is of importance and has been used to explain the production of a turbulent pressure field (see Kraichnan[4] and Fuchs[5]). This relationship was pursued by Planchon[3] for a simple jet and extended to nonzero velocity ratio cases in this work. The investigation produced the general expression

$$\frac{p'_{T-M}}{\tfrac{1}{2}\rho\bar{U}_1^2(1-r)^2} = 2\left[\frac{8}{15}\right]^{1/2}\left[\left|\frac{\partial\bar{U}/\bar{U}_1^{(1-r)}}{\partial y}\right| \times (x-x_0)\right]\left[\frac{v'}{\bar{U}_1(1-r)}\right]\left[\frac{L_{vv}^y}{x-x_0}\right]A \qquad (2)$$

where $pT-M$= contribution to the rms of the pressure fluctuations from the turbulent-mean shear interaction, in contrast to a turbulent-turbulent interaction

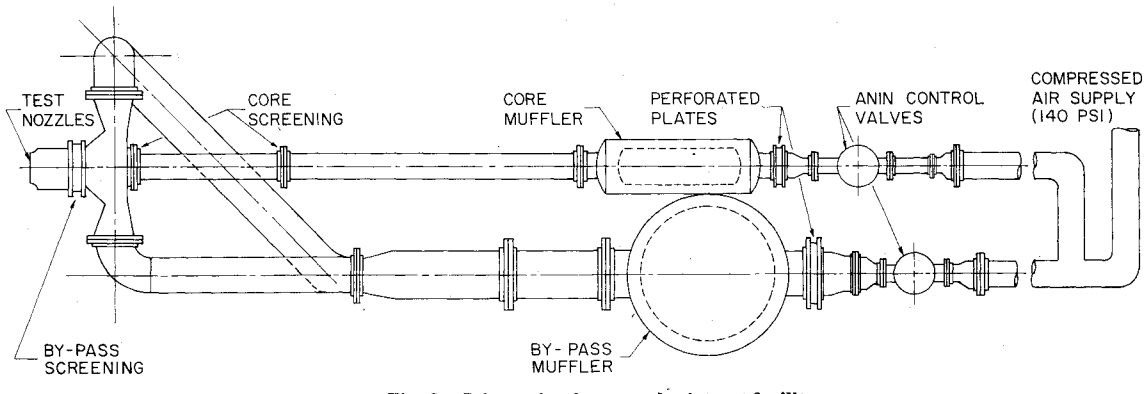

Fig. 2 Schematic of co-annular jet test facility.

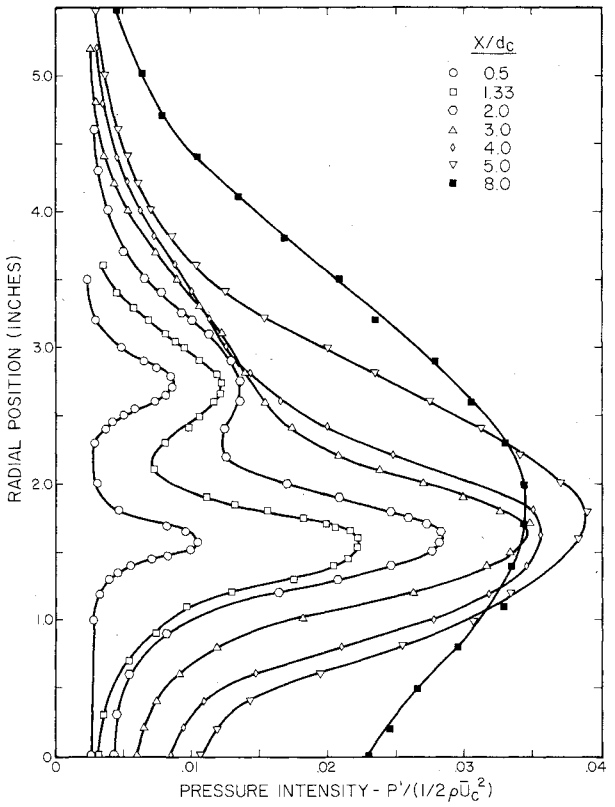

Fig. 3 Fluctuating pressure intensity radial profiles. $U_c = 450$ fps; $\bar{U}_{Bp} = 180$ fps; $d_c = 3.0$ in.; $d_{Bp} = 5.35$ in.

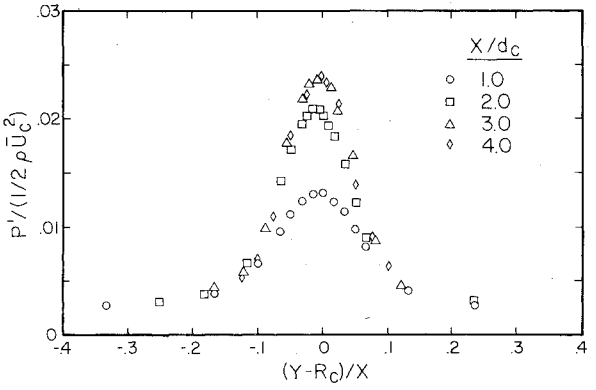

Fig. 4 Pressure intensity similarity profiles. $\bar{U}_c = 450$ fps; $\bar{U}_{Bp} = 180$ fps; $d_c = 3.0$ in.; $d_{Bp} = 8.7$ in.

$$\left| \frac{\partial [\bar{U}/\bar{U}_1 (1-r)]}{\partial y} \right| (x - x_0)$$

= nondimensionalized mean velocity gradient $v'/\bar{U}_1 (1-r)$ = radial velocity component intensity; $L^y{}_{vv}/(x-x_0)$ = normalized radial velocity radial integral length scale; A = anisotropy factor, which accounts for the lack of isotropy in a shear flow; r = velocity ratio, $\bar{U}_2/\bar{U}_1$, where $\bar{U}_1$ and $\bar{U}_2$ are the high velocity and low velocity streams, respectively, for a general mixing layer.

The pressure field results from two different types of contributions manifested by the velocity field. These contributions are the turbulent-turbulent (T-T) and turbulent-mean shear (T-M) interactions that occur in the turbulent velocity field. In the case of a mixing layer, the turbulent-mean shear term dominates over the turbulent-turbulent term in the heavily sheared central portion of the mixing layer. This is the portion of the flow where Eq. (2) is applied. The necessary assumptions and approximations are detailed by

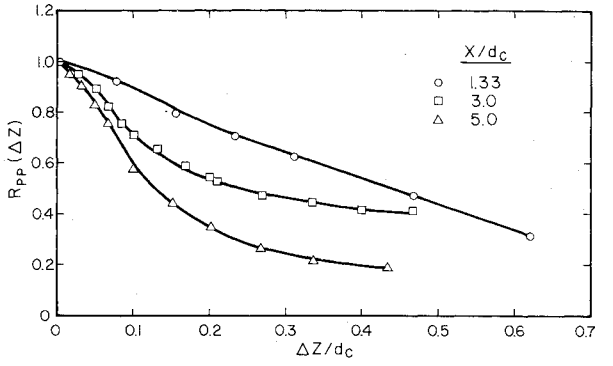

Fig. 5 Lateral space correlations for pressure. $\bar{U}_c = 450$ fps; $\bar{U}_{Bp} = 180$ fps; $d_c = 3.0$ in.; $d_{Bp} = 5.35$ in.; $y/R_c = 1.0$.

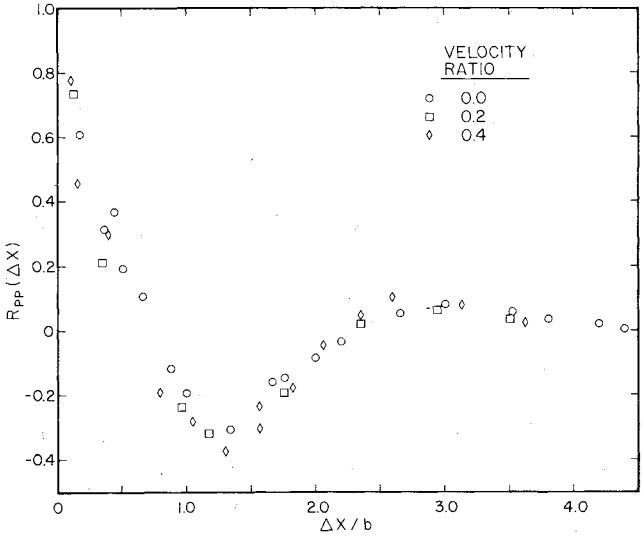

Fig. 6 Axial space correlations for pressure. $\bar{U}_c = 450$ fps; $d_c = 3.0$ in.; $d_{Bp} = 5.35$ in.; $x/d_c = 1.33$; $y/R_c = 1.0$.

Planchon[3] and are not repeated here. The significant result exhibited by this expression is that the fluctuating pressure field is produced by the radial velocity component alone, at least in the central highly sheared region of a mixing layer. The accuracy of this prediction is within +17% to −11% of the measured values. Although additional data are necessary for verification, the accuracy of the prediction does appear to be dependent upon velocity ratio.

Two-Point Pressure Correlation

A normalized correlation coefficient (R_{pp}) was determined by dividing the covariance of the output from the two sensors by the respective local rms value of each sensor. Stated mathematically, in general terms

$$R_{pp}(x,y,z,\Delta x,\Delta y,\Delta z,\eta_0,\tau) = \frac{\overline{p(x,y,z,\eta_0,t)\,p(x+\Delta x,y+\Delta y,z+\Delta z,\eta_0,t+\tau}}{\left[\overline{p^2(x,y,z,\eta_0,t)}\;\overline{p^2(x+\Delta x,y+\Delta y,z+\Delta z,\eta_0,t+\tau)}\right]^{1/2}} \quad (3)$$

The filtered fluctuating pressure at center frequency η_0, at a point (x,y,z,t) is correlated with the filtered fluctuating pressure at a point removed from it by $\Delta x, \Delta y, \Delta z, \tau$. The over bar denotes the long-time average of a statistically stationary quantity. In subsequent presentations only nonzero separations will be entered as arguments and η_0 will be omitted for broad-band correlations.

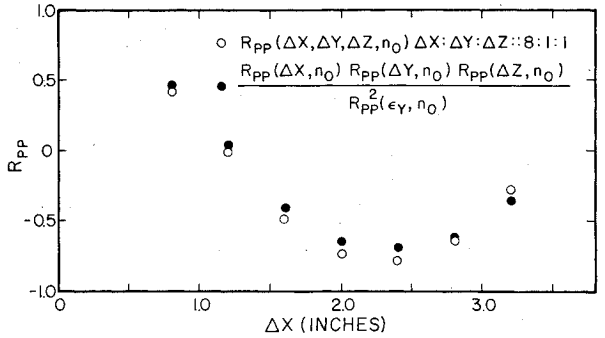

Fig. 7 Verification of spatial separability. $\bar{U}_c = 450$ fps; $\bar{U}_{Bp} = 360$ fps; $d_c = 3.0$ in.; $d_{Bp} = 5.35$ in.; $x/d_c = 1.33$; $\eta_0 = 500$ Hz.

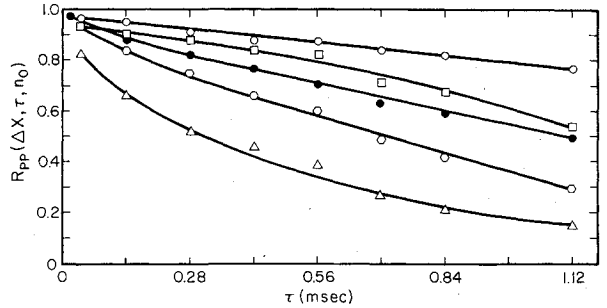

Fig. 8 Narrow-band convected frame auto-correlations. $r = 0.4$; ∘ $\eta_0 = 2$KHz; □ $\eta_0 = 3$KHz; ◇ $\eta_0 = 4$KHz; $\Delta\eta_0 = 5$Khz; $x/d_c = 1.33$; $y/R_c = 1.0$; $d_c = 3.0$ in.; ● All pass.

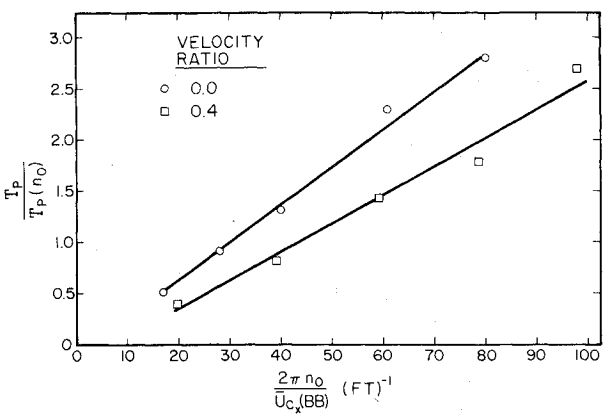

Fig. 9 Narrow-band convected frame integral time scales. ∘ $\bar{U}_{c_x}$ (BB) = 111 fps; $T_p = 2.76$ msec and □ $\bar{U}_{c_x}$ (BB) = 320 fps; $T_p = 1.5$ msec; $x/d_c = 1.33$; $y/R_c = 1.0$; $d_c = 3.0$ in.

Three special cases of Eq. (3) corresponding to axial, radial, and lateral separations were measured. In addition, three dimensional or "offdiagonal" separations were made. These measured data were analyzed as broad-band and as narrowband signals. The special case of $\tau = 0$ was evaluated to yield space correlations. The variations in delay-time τ and spatial separation were used to infer convection velocities.

Initially, the broad-band space correlations were investigated. As predicted by Kraichnan[4] and observed by Scharton and White[6] and others, for pressure the axial space correlation differs markedly from the radial and lateral space correlations. The lateral space correlations shown in Fig. 5 demonstrate an exponential form for small separations and an inverse power law dependence for large separations. The radial space correlations display a similar dependence on separation distance. In contrast, the axial space correlations shown in Fig. 6 are characterized by an exponentially damped cosine behavior. The extent of the exponential dependence of the radial and lateral space correlations varied between 35% and 50% for a large range of flow conditions. This region is assumed to be a manifestation of the hydrodynamic pressure field within the jet flow. The axial space correlations are described by two parameters: 1) a damping coefficient, and 2) a wavelength of periodicity λ. L^x_p was found to be independent of position and flow conditions. However, λ was found to grow linearly with increasing axial position and to be dependent upon the flow conditions. Thus, the expression

$$\lambda = \lambda_c(x - x_0) \tag{4}$$

was adopted in which λ_c is dependent upon the velocity ratio. The value of λ_c was found to be 0.30 for zero velocity ratio and 0.25 for 0.4 velocity ratio. References 1 and 3 discuss the dependencies of L^x_p and λ_c more completely. Since the mixing layer width b also varies linearly with axial position, $\Delta x/b$ would be expected to collapse results for different velocity ratios. This is clearly shown in Fig. 6.

The spatial separability of the three-dimensional space correlation was investigated. Such separability implies that

$$R_{pp}(\Delta x,\Delta y,\Delta z,\eta_0) = R_{pp}(\Delta x,\eta_0)\,R_{pp}(\Delta y,\eta_0)\,R_{pp}(\Delta z,\eta_0) \tag{5}$$

The validity of this form was checked by comparing the product of the three individual spatial correlations to the corresponding "off-diagonal" results. Figure 7 verifies the validity of Eq. (5). This is a very useful result since it allows for the correction of the probe offset required by experimental limitations. The correlation data were acquired using a radial probe offset ϵ_y. The effect of ϵ_y is nullified by dividing a correlation function, e.g. $R(\Delta x,\epsilon_y,\eta_0)$, by the value of $R_{pp}(\Delta y,\eta_0)$ corresponding to $\Delta y = \epsilon_y$. This correction technique is further emphasized by the nomenclature in Fig. 7.

It is important to recognize the generality of the foregoing comments about the two-point structure of the pressure field. These results apply to both zero and nonzero velocity ratio mixing layers and are independent of area ratio. Further, the observations are equally applicable to broad-band and narrow-band correlations. It is further noted that the data encompassed the full length of the mixing regions and extended into the final transition region ($x/d_c = 6$).

Convected Frame Pressure Field

The pressure field was found to have only an axial convection velocity as the radial and lateral space-time correlations displayed zero convection velocities. The axial convection velocity was observed to be essentially constant across the mixing layer and, further, to be nearly constant for the first six core diameters, and equal to the mean velocity at the centerline of mixing. These observations are valid for velocity ratios ranging from 0.0 to 0.8.

The narrow-band convection velocities were also calculated. They showed that the various frequency components are convected at different speeds. For the centerline of mixing, the low-frequency or large eddies travel slower than the high-frequency or small eddies. Further, the large eddies convect at about the velocity of the centerline of mixing, while the small eddies have a convection velocity comparable to the local mean velocity.

The broad-band and narrow-band convected frame integral time scales were calculated from the space-time correlation data. Figure 8 shows a set of narrow-band convected-frame autocorrelations for several frequencies. The broad-band result has been included for comparison. The characteristic frequency (η_{50} = frequency which divides the spectral energy content in half) for this data set was 2000 Hz. Figure 8 shows that the large eddies persist for a larger distance downstream than the small eddies. The general shape of these curves is exponential and such a form was used to estimate the integral time scales, $T_p(\eta_0)$, i.e.

$$R^L_{pp}(\eta_0,\tau) = \exp[-\tau/T_p(\eta_0)] \tag{6}$$

The broad-band and narrow-band integral time scales were constant across the mixing layer for a given axial position. Their axial variation is not easily scaled, but was found to decrease for the extent of the mixing regions. Further, the broad-band integral time scale for pressure was relatively large. In fact, it was nearly twice as large as the integral time scale of the axial velocity component.

The narrow-band integral time scales are seen to be linearly proportional to a length scale of wave number $2\pi\ \eta_0/\bar{U}_{c_x}$ (BB), in Figure 9. The linear relationship holds for both the low-and middle-range frequencies and is consistent with the rather standard idea of fixed-frame frequencies being associated with given eddy sizes. This concept is valid as long as the frequencies are sufficiently low that viscous dissipation effects are small. It also applied to velocity field results. Figure 9 shows the results for two mixing regions of different velocity ratios. These curves collapse onto one if the width of the mixing layer b is incorporated into the abscissa, $2\pi\ \eta_0\ b/\bar{U}_{c_x}$ (BB). The broad-band axial convection velocity, $\bar{U}_{c_x}$ (BB) is used in this relation.

Narrow-Band Space-Time Correlation Model

The observed functional forms of the space correlations and the existence of spatial separability may be used to synthesize a model for the narrow-band space-time correlation function. The resulting expression is

$$R_{pp}\ (\Delta x,\Delta y,\Delta z,\eta_0,\tau)$$

$$=\exp\left\{-\frac{2\pi\eta_0}{\bar{U}_{c_x}(\eta_0)}\left[K_x(\Delta x-\tau\bar{U}_{c_x}(\eta_0))+K_y\Delta y+K_z\Delta z\right]\right\}$$

$$\cos\left\{\frac{2\pi\eta_0[\Delta x-\tau\bar{U}_{c_x}(\eta_0)]}{\bar{U}_{c_x}(\eta_0)}\right\}\exp-\left\{\frac{[\tau-\Delta x/\bar{U}_{c_x}(\eta_0)]}{T_p(\eta_0)}\right. \tag{7}$$

This form is for the stationary frame and the axial coordinate accounts for the convective effects. The time dependence is simply incorporated by an exponential decay, i.e., the autocorrelation of the convected frame. K_x,K_y, and K_z are decay coefficients which are determined as follows:

$$K_x=1/2\pi\eta_0\ T_p(\eta_0) \tag{8}$$

$$K_y=\bar{U}_{c_x}(\eta_0)\ /2\pi\ \eta_0 L_p{}^y\ (\eta_0) \tag{9}$$

$$K_z=\bar{U}_{c_x}(\eta_0)\ /2\pi\ \eta_0 L_p{}^z(\eta_0) \tag{10}$$

A special case would be the axial narrow-band space-time correlation formed by setting Δy and Δz equal to zero in Eq. (7). The axial functional form is compared to the actual measured correlation in Fig. 10. The agreement for both the location of the peak correlation and the shape of the curves is good. A similar comparison was made by Planchon,[3] but for broad-band data. His results also gave good agreement for the magnitude and placement (in time) of the peaks in the space-time correlation curves. However, his predicted curves were markedly narrower than the measured ones. This result was attributed to a dispersive effect that broadens the space-time correlation curve. The dispersive effect could be a result of the various size eddies having different convection speeds. Further, as the turbulence pattern is convected downstream, the smaller eddies are dissipated. Thus, the flow is composed mostly of the large, slow-moving eddies. The effect of this condition is to broaden the space-time correlation for larger delay times. This is not the case when only an individual frequency component's behavior is considered. Thus, the narrow-band space-time correlations do not display significant dispersive effects. Therefore, the final conclusion

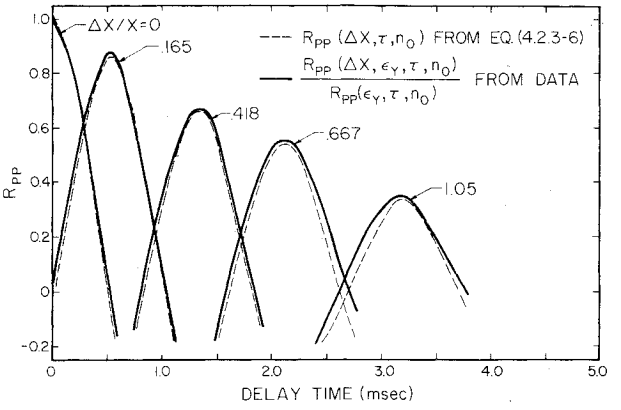

Fig. 10 Axial space-time narrow-band pressure correlation. $x/d=1.33$; $\eta_0=500$ Hz; $\bar{U}_{Bp}=180$ fps; $d_c=3.0$ in.; $d_{Bp}=5.35$ in.; $y/R_{Bp}=1.0$.

is that the narrow-band correlations do demonstrate spatial and temporal separability and are adequately represented by Eq. (7).

IV. Conclusions

This investigation has encompassed both single-and two-point turbulent structure of the fluctuating pressure field in a co-annular nozzle configuration. Several major conclusions are reached with respect to this pressure field, its structure and its characteristics.

1) The pressure intensity due to turbulent-mean shear interactions can be predicted from velocity field data—in particular, v' and $\partial\bar{U}/\partial y$.

2) The radial and lateral space correlations are fundamentally different from the axial space correlation.

3) Spatial separability is valid for both broad-band and narrow-band data and is independent of area or velocity ratios.

4) The narrow-band space-time correlations are separable in both space and time.

5) An acceptable model for the narrow-band space-time correlation function has been formulated.

6) The pressure field structure has a nonzero convection velocity only for the axial direction.

7) The effect of velocity ratio has been accounted for by utilizing the width of the mixing layer b as a length scale to collapse results from different velocity ratios.

The general nature of the flowfield that evolves from this investigation can be applied to the prediction of aerodynamic jet noise. For example, the three distinct zones observed in the co-annular flow should be treated as independent sound sources. The expressions for the space-time correlation (Eq. (7)] and the local pressure intensity [Eq. (1)] can be combined to form a relation for the pressure field's covariance. This quantity is exactly the source term in Ribner's[2] formulation of the aerodynamic noise produced by a turbulent pressure field. These direct applications and other more subtle points are discussed by Hammersley[1] and are the subject of a paper in preparation.

References

[1]Hammersley, R.J., "An Experimental Investigation of the Turbulent Characteristics of Co-Annular Jets and Their Role in Aerodynamic Noise Generation," Ph.D. Thesis, Nuclear Engineering Program, University of Illinois, Urbana, Ill. 1974.

[2]Ribner, H.S. , "The Generation of Sound by Turbulent Jets," *Advances in Applied Mechanics,* Vol. 8, H.L. Dryden, T. VonKarman, and G. Kuerti, Academic Press, New York, 1964, pp. 103-187.

[3]Planchon, H.P. Jr., "The Fluctuating Static Pressure Field in a Round Jet Turbulent Mixing Layer," Ph.D. Thesis, Nuclear Engineering Program, University of Illinois, Urbana, Ill. 1974.

[4]Kraichnan, R.H., "Pressure Field within Homogeneous Anisotropic Turbulence," *The Journal of the Acoustical Society of America,* Vol. 28, 1956, pp.64-72.

[5]Fuchs, H.V., "Measurement of Pressure Fluctuations with Microphones in an Airstream" Institute of Sound and Vibration Research, Memorandum 281, University of Southampton, 1969.

[6]Scharton, T.D. and White, P.H., "Simple Pressure Source Model of Jet Noise," *Journal of the Acoustical Society of America,* Vol. 52, July 1972, pp. 399-412.

From the AIAA Progress in Astronautics and Aeronautics Series . . .

METHODS IN ASTRODYNAMICS AND CELESTIAL MECHANICS—v. 17

Edited by Raynor L. Duncombe, U. S. Naval Observatory, and Victor G. Szebehely, Yale University Observatory

The nineteen papers in this volume deal with applications of the methods of celestial mechanics to problems of space engineering, including the behavior of bodies near libration points, asymptotic representations of space vehicle trajectories, orbit determination and mission analysis, and optimization in astrodynamics.

Papers discuss libration around equilibrium positions and in a three-body system, with a critical review of the literature. Motion at libration points in the earth-moon system, and the stability of equilibrium solutions, are also discussed.

Other papers treat trajectory representation, perturbation mechanics, interplanetary trajectory computation, close satellite motion in the restricted three-body problem, and an asymptotic basis of satellite orbit perturbation mechanics. Orbit prediction and determination, error equation generation, multistep algorithms, two-point boundary problems, with a number of possible procedures, are also considered.

Other papers apply algorithms to nonlinear two-point boundary problems, present trajectory optimization by a variety of methods, and solve optimal control problems.

436 pp., 6 x 9, illus. $11.00 Mem. & List

TO ORDER WRITE: Publications Dept., AIAA, 1290 Avenue of the Americas, New York, N. Y. 10019